

See discussions, stats, and author profiles for this publication at: <https://www.researchgate.net/publication/49706118>

# Electric Field Dependent Photocurrent Decay Length in Single Lead Sulfide Nanowire Field Effect Transistors

ARTICLE in NANO LETTERS · FEBRUARY 2011

Impact Factor: 13.59 · DOI: 10.1021/nl1038456 · Source: PubMed

---

CITATIONS

41

---

READS

72

4 AUTHORS, INCLUDING:



Eunsoon Oh

Chungnam National University

102 PUBLICATIONS 1,118 CITATIONS

SEE PROFILE



Dong Yu

University of California, Davis

38 PUBLICATIONS 1,243 CITATIONS

SEE PROFILE

# Electric Field Dependent Photocurrent Decay Length in Single Lead Sulfide Nanowire Field Effect Transistors

Rion Graham,<sup>†,§</sup> Chris Miller,<sup>†,§</sup> Eunsoo Oh,<sup>‡</sup> and Dong Yu<sup>\*,†</sup>

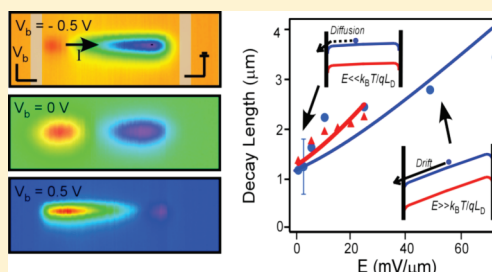
<sup>†</sup>Department of Physics, University of California, Davis, California 95616, United States

<sup>‡</sup>Department of Physics, Chungnam National University, Daejeon, 305-764, Korea

 Supporting Information

**ABSTRACT:** We determined the minority carrier diffusion length to be  $\sim 1 \mu\text{m}$  in single PbS nanowire field effect transistors by scanning photocurrent microscopy. PbS nanowires grown by the vapor–liquid–solid method were p-type with hole mobilities up to  $49 \text{ cm}^2/(\text{V s})$ . We measured a photoresponse time faster than  $14 \mu\text{s}$  with near-unity charge separation efficiency at the contacts. For the first time, we also observed a field-dependent photocurrent decay length, indicating a drift dominant carrier transport at high bias.

**KEYWORDS:** PbS, nanowires, field effect transistors, scanning photocurrent microscopy, minority carrier diffusion length, solar cells



Semiconductor nanostructures with narrow band gaps, including PbS and PbSe, have recently garnered much attention as building blocks for photovoltaic devices.<sup>1–3</sup> Narrow band gap semiconductors are excellent infrared absorbers and can be used in a multijunction solar cell to collect the infrared light that constitutes half of the total solar energy spectrum.<sup>4</sup> In addition, the large Bohr radii of narrow band gap semiconductors also lead to strong quantum confinement effects that tailor the band gap for maximum efficiency.<sup>1</sup> Highly efficient multiexciton generation (MEG) in narrow band gap quantum dots (QDs) may lead to an efficiency beyond the Shockley and Queisser limit of  $\sim 31\%$ .<sup>5,6</sup> Nanowires (NWs) provide much more efficient transport channels for photocarrier extraction compared with QDs, enabling more efficient charge collection. Photovoltaic devices built upon dense and vertical NW arrays take advantage of this efficient charge separation at large nanostructure interfaces. The length of the NWs ensures that the cell is optically dense, while the minority carriers travel radially to cross the junction.<sup>7</sup> This geometrical advantage greatly relieves the demand on the long diffusion length of the minority carriers; thus, even average quality (low cost) materials in NW form can make efficient solar cells. For the optimal design of this type of NW solar cell, knowledge of the minority carrier diffusion length ( $l_D$ ) is particularly valuable, as this length dictates the maximum NW diameter in an efficient solar cell. If  $l_D$  is much shorter than the NW diameter, the minority carriers recombine before diffusing to the interface, resulting in a low charge separation efficiency. An  $l_D$  of  $\sim 2 \mu\text{m}$  has been measured in Si NWs;<sup>8</sup> however, to our knowledge,  $l_D$  has not been measured in narrow band gap semiconductor NWs.

Scanning photocurrent microscopy (SPCM) is a valuable experimental technique that allows for extraction of carrier diffusion lengths and local electronic band bending.<sup>8–17</sup> In a

SPCM setup, a tightly focused laser is raster scanned at the surface of a planar electronic device, while the photocurrent is recorded as a function of illumination position. This technique has been recently employed to investigate single carbon nanotube and semiconductor NW devices. In carbon nanotubes, the carrier lifetime is  $\sim 30 \text{ ps}$ .<sup>18</sup> This fast recombination leads to an ignorable carrier density gradient and small diffusion current. Experimental SPCM images show photocurrent spots are localized near the contacts, where the electric field is large because of a Schottky barrier.<sup>9,13</sup> On the other hand, in semiconductor NWs, recombination rates are much slower and diffusion plays an important role. The photocurrent spots are often elongated with an exponential decay that has been used to estimate the minority carrier diffusion length.<sup>8,11,15</sup> Interpretation of SPCM results in semiconductor NWs is therefore not as straightforward as in carbon nanotubes because of the electric field redistribution associated with the separation of the injected carriers. To date, most SPCM studies on NWs are either on devices with large contact barrier<sup>8</sup> or space charge limited transport,<sup>11</sup> while the effect of the external electric field to the photocarrier separation and transport is not well understood in Ohmic NW devices. In addition, there has been no detailed study on SPCM measurement of narrow band gap semiconductor NWs,<sup>16</sup> which may provide new insights on the mechanism of the separation and transport of photogenerated charge carriers for two reasons: (1) PbS has a very large dielectric constant (172) and thus a strong electrostatic screening, leading to a long carrier lifetime ( $63 \mu\text{s}$  in intrinsic PbS<sup>19</sup>) and an expected long diffusion length; (2) PbS has a narrow band gap (0.41 eV) such that we expect to achieve

**Received:** November 1, 2010

**Revised:** December 15, 2010

**Published:** December 23, 2010

ambipolar doping in PbS NW-FETs and investigate the diffusion/drift lengths and band bending as a function of the carrier type and concentration.

Here we explored the optoelectronic properties of field effect transistors (FETs) incorporating single PbS NWs grown by the vapor–liquid–solid (VLS) approach with the SPCM technique. The FETs exhibited strong gate dependence with hole mobilities up to  $49 \text{ cm}^2/(\text{V s})$  at room temperature. With the use of Cr electrodes and HF etching, we achieved Ohmic contact with the p-type PbS NWs and expect the electric field to be uniformly distributed along the NW. From the SPCM measurements, we observed a downward band bending toward the contact, which flipped direction at high gate voltages. The photocurrent decayed exponentially with the injection position, from which an electron (minority carrier) diffusion length of  $\sim 1 \mu\text{m}$  was extracted. Remarkably, the photocurrent decay length increased with bias, different from the reports in CdS and Si NWs,<sup>8,11</sup> where the decay lengths were independent of bias voltage. We attribute this increase to a transition from diffusion to drift-dominated photocurrent under high electric field.

Single crystalline PbS NWs were synthesized via the vapor–liquid–solid (VLS) mechanism following a slightly modified recipe as described in ref 20. Briefly,  $\text{PbCl}_2$  powder (99.999%, Alfa Aesar) was placed at the center of a horizontal tube furnace and S powder (99.9999%, Alfa Aesar), in a 1:2 ratio, was placed upstream just outside the mouth of the furnace. The quartz tube was purged with dry  $\text{N}_2$  three times, followed by a continuous flow of  $\text{N}_2$  at 150 SCCM. The furnace temperature was then raised to  $650^\circ\text{C}$  with a rate of  $40^\circ\text{C}/\text{min}$ . At the peak temperature, 1 SCCM of  $\text{H}_2$  was introduced to reduce  $\text{PbCl}_2$  to Pb catalytic nanoparticles and the S powder was immediately moved into the furnace. After 1 min, the  $\text{H}_2$  flow was turned off and the furnace remained at its peak temperature for 15 min, followed by a rapid cooling to room temperature. The deposition occurred on the Si(100) substrate that was placed 10 cm downstream from the center. The growth resulted in hyperbranched NW clusters with NW diameters ranging from 50 to 125 nm and lengths up to tens of micrometers. Energy-dispersive X-ray spectroscopy (EDS) showed that the NWs are composed of 1:1 Pb and S. X-ray diffraction (XRD) confirmed they were crystalline and had a rock-salt structure (Figure S1 in the Supporting Information).

As-grown NWs were sonicated in methanol to form a suspension, which was drop-cast onto a 300 nm  $\text{SiO}_2$  covered, highly doped p-type Si wafer (purchased from University Wafer). Electrical contacts were defined using an FEI 430 NanoSem EBL system. After development, the contact area was first cleaned by Ar plasma (60 s, 600 V  $\times$  2 nA) to remove excess resist and then etched in a 6:1 buffered HF for 6 s. The device fabrication was completed by immediate electron beam deposition of 75 nm Cr/75 nm Au and liftoff. The HF treatment led to a more than 500-fold increase in the device conductance (Figure 1a). The current saturation at higher bias in untreated devices can be understood by considering two back-to-back diodes. Earlier reports have shown that as-grown PbS NWs are coated by a silica layer,<sup>21</sup> which can be removed by HF treatment, thereby reducing the contact barrier. Typical devices (such as D1) exhibited a nearly Ohmic current–voltage ( $I$ – $V$ ) characteristic. Four probe measurements confirmed the contact resistance was  $<1\%$  that of the NW. A negative gate voltage ( $V_g$ ) led to an increase in conductivity, implying the NW was p-type (Figure 1b). The hole mobility,  $\mu_p$ , was estimated to be  $49 \text{ cm}^2/(\text{V s})$  and the hole concentration,  $p$ , to be  $3.2 \times 10^{18} \text{ cm}^{-3}$ . Applying  $V_g$  up to 100 V

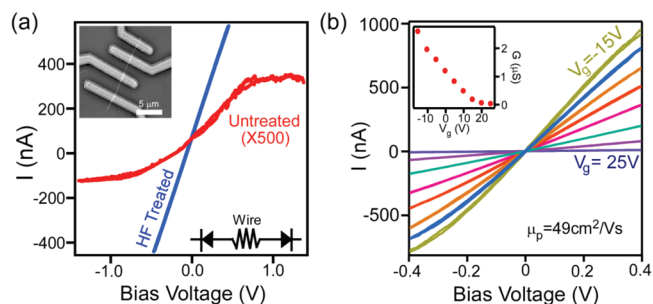


**Figure 1.** Device image and current–voltage characteristics. (a)  $I$ – $V$  curves of a representative NW before (red) and after (blue) treatment in 6:1 buffered oxide etch (BOE) to remove the silica sheath from the NW at the electrode contacts. Inset: SEM image of the NW with four-probe electrode configuration. Bottom: The NW device is modeled by a resistor connected to back-to-back diodes. (b) Back gate dependent  $I$ – $V$  curves of a NW after the BOE treatment ( $V_g = 25, 15, 10, 5, 0, -5, -10, -15 \text{ V}$ , respectively). Inset: NW conductance as a function of back gate voltage.

resulted in ambipolar conduction in only a few devices (Figure S2b in the Supporting Information). An electron mobility of  $0.5 \text{ cm}^2/(\text{V s})$  was observed in the ambipolar devices. All 20 devices measured from different synthetic batches showed p-type doping with carrier concentration between  $10^{17}$  and  $10^{19} \text{ cm}^{-3}$ . Our NWs appear to be doped more lightly than the samples grown by a similar method in ref 22, presumably due to the subtle difference in synthetic conditions.

Optoelectronic measurements were performed using the SPCM setup shown schematically in Figure 2a. A Coherent 532 nm continuous wave laser was focused onto the device by a NA0.95  $100\times$  objective lens in a BX51 Olympus microscope. The diameter of the focused spot was  $\sim 1 \mu\text{m}$  as determined from the SPCM cross section perpendicular to the NW. In the following polarization, intensity dependence, and response time measurements, we fixed the bias voltage ( $V_b$ ) to be zero and focused the laser spot on one of the contacts. First, the photocurrent was measured as a function of linear polarization angle, giving an anisotropy ratio of 0.41 (Figure 2b). The anisotropy ratio is defined by  $(I_{\parallel} - I_{\perp})/(I_{\parallel} + I_{\perp})$ , where  $I_{\parallel}$  ( $I_{\perp}$ ) is the photocurrent when incident electric field is parallel (perpendicular) to the orientation of the NW. Given the high dielectric constant, 172, of PbS, a near-unity ratio is expected.<sup>23</sup> The smaller measured value may be due to the finite NW diameter and light scattering at the contacts. We then measured photocurrent vs illumination intensity, which was estimated from the total laser power measured underneath the objective lens divided by the circular area of the laser spot ( $d_{\text{laser}} = 1 \mu\text{m}$ ). The photocurrent increased linearly below  $200 \text{ W}/\text{cm}^2$  and was proportional to the square root of intensity at higher values (Figure 2c). We attribute the non-linearity at high intensity to increased recombination rates due to high photocarrier density. In the following measurements, our laser intensity was always kept in the linear region.

By modulating the laser beam with a chopper at 1 kHz (Thorlabs), the photocurrent 10–90% rise time was measured to be  $14 \mu\text{s}$ , with a zero-bias photocurrent of  $1.8 \text{ nA}$  at an intensity of  $50 \text{ W}/\text{cm}^2$  (Figure 2d). An equally fast fall time was measured, with neither response time depending on the bias or gate voltages. Importantly, the measured response time was an upper-bound value since the measurement was limited by the rise time of the preamplifier ( $\sim 20 \mu\text{s}$  at the sensitivity of  $10^{-6} \text{ A/V}$ , DL Instruments, model 1211) and/or the beam cutting time by the

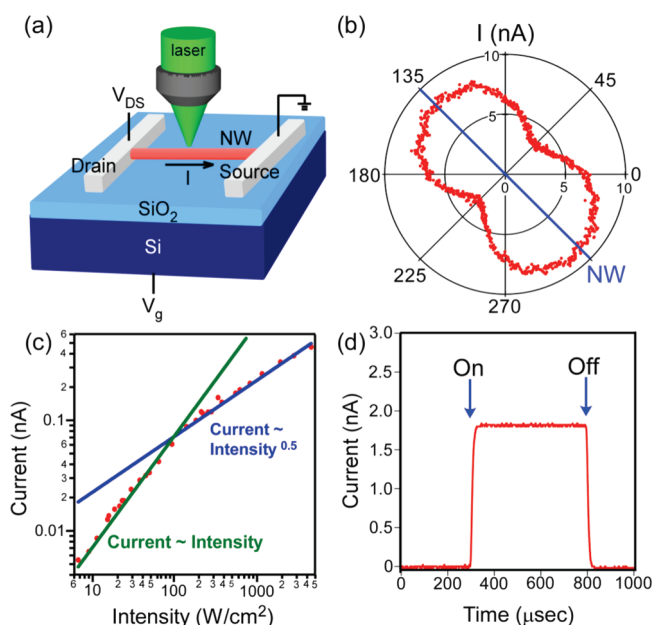


**Figure 2.** Optoelectronic characterization of single PbS NW FETs (all measurements performed at  $V_b = 0$  V and with the laser spot focused at one of the NW–metal contacts). (a) Schematic of scanning photocurrent microscopy (SPCM). (b) Photocurrent as a function of linear polarization angle. Photocurrent from the NW (represented by the blue line) is maximized when the polarization is parallel with the NW and minimized when it is perpendicular, leading to an anisotropy ratio of 0.41. (c) Photocurrent as a function of laser intensity. The photocurrent responds linearly with intensity for values below  $200 \text{ W/cm}^2$ , and as the square root for those above. (d) Temporal response of photocurrent from laser modulated with a chopper at 1 kHz. The arrows indicate the time at which the NW is first exposed to light and last exposed to light.

chopper ( $\sim 30 \mu\text{s}$  estimated from the beam size and the blade rotation speed). Further measurements must be conducted to determine the actual response time of the NWs. The observed photoresponse of  $<14 \mu\text{s}$  is one of the fastest in NW photodetectors.<sup>24,25</sup> Most NWs have shown much slower response times, ranging from milliseconds to seconds.<sup>26</sup> The slow response is generally attributed to charge carrier trapping at surface states. The fast response time indicates that our NWs are nearly free of slow charge traps, possibly because of the silica coating.

Before discussing the spatial distribution of the photocurrent, we first focus on the charge separation efficiencies at the photocurrent peaks. Our NW-FETs demonstrated high charge separation efficiencies, estimated from  $\eta_{cc} = I/qF$ , where  $F$  is the absorbed photon flux.<sup>27</sup> At  $V_g = -10$  V, the maximum magnitude of the photocurrent was 30 nA (Figure 3c) at the incident power  $P_0 = 1.5 \mu\text{W}$  (intensity  $I_0 = 190 \text{ W/cm}^2$ ) in device **D1**, yielding a charge separation efficiency of  $\sim 72\%$ .  $\eta_{cc}$  decreased to a minimum as  $V_g$  was increased to 50 V and increased again to  $\sim 80\%$  at  $V_g = 90$  V. The gain,  $G$  (carriers passing through the NW per photon absorbed), was measured in a different device, **D3**, under bias. At  $V_b = 0.75$  V,  $G$  was estimated to be 6.5, with incident power  $0.25 \mu\text{W}$  and photocurrent 46 nA (Figure 4b). All these tests demonstrate that PbS NWs can serve as fast, sensitive, and polarization-dependent nanoscale infrared/visible photodetectors.

SPCM images of a typical device **D1** at various  $V_g$  values are shown in Figure 3. At  $V_b = V_g = 0$ , among all 20 devices measured,

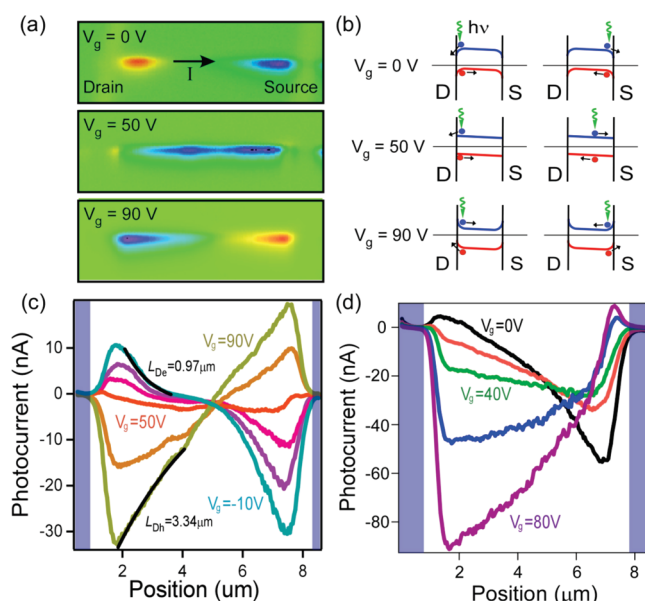


**Figure 3.** Gate dependence of the SPCM: (a–c) for device **D1** with a 75 nm diameter PbS NW; (d) for device **D2**. Both measurements were performed with  $V_b = 0$  V and excitation power  $1.5 \mu\text{W}$ . (a) Photocurrent as a function of laser spot position, overlaid by the reflection image of the electrodes connected to the NW, at different  $V_g$ . The positive current direction is from left to right as indicated. Note that the color scales are different in the three images. (b) The corresponding band diagrams for each  $V_g$  describing the photocurrent generation. (c) Line scans of photocurrent from part a as a function of gate voltage ( $V_g = 90, 50, 30, 10, -10$  V respectively). (d) Line scans of photocurrent for a different device **D2** as a function of gate voltage ( $V_g = 0, 20, 40, 60, 80$  V, respectively).

photocurrent was always positive (negative) near the drain (source). Photocurrent spots in SPCM images have been attributed to local electric fields at the contact Schottky barriers.<sup>10</sup> The signs of the photocurrent near the contacts at  $V_g = 0$  V are in agreement with downward band bending toward the metal contact, consistent with the work function of Cr (4.5 eV) being smaller than the ionization potential of PbS ( $\sim 4.95$  eV as in ref 28). The Schottky barrier height is determined not only by the metal work function but also by the surface states of the semiconductor and has to be measured experimentally. In device **D1**, when fixing  $V_b = 0$  and increasing  $V_g$ , the magnitude of photocurrent near both contacts was reduced. As  $V_g$  reached a threshold voltage  $\sim 50$  V (17–70 V varying from device to device), the photocurrent “spot” was extended to nearly the entire length of the wire with a greatly reduced magnitude. As  $V_g$  kept increasing to 90 V, the photocurrent spots were again localized at the contacts, but with an opposite polarity. The reverse of the photocurrent at positive  $V_g$  indicates that the band bending direction flips (Figure 3b), driven by large  $V_g$ . The electric field associated with this bending at the contacts leads to an efficient charge separation. At the turning point from downward to upward band bending, the photocurrent becomes very small, signaling a weak field, or flat band, at the contacts. At this threshold voltage, a low magnitude, elongated photocurrent appears along almost the entire NW, most likely due to an electric field caused by the slight difference in the barrier heights at each contact. This is supported by the asymmetry in the magnitude of the photocurrent at the contacts.



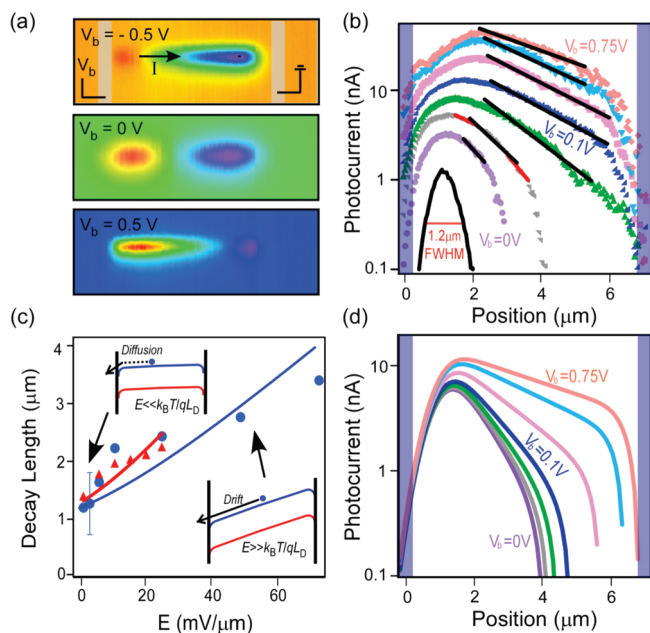


**Figure 4.** Bias dependence of the SPCM for device D3. (a) Photocurrent images of the NW as a function of  $V_b$ . The left electrode (drain) is connected to the bias voltage source ( $V_b$ ) and the positive current direction is from left to right as indicated. Note that the color scales are different in the three images. (b) Log-scale line scans of photocurrent with excitation power  $0.25 \mu\text{W}$  at  $V_b = 0, 0.02, 0.05, 0.1, 0.25, 0.5, 0.75$  V, bottom to top. The shaded areas are metal electrodes. The exponential fits enable extraction of the photocurrent decay length. (c) The photocurrent decay length extracted from two NW devices vs external electric field. The error bar was estimated from fitting different ranges as shown by the red fitting curves in (b). The fits by eq 1 yield  $l_D = 1.0 \mu\text{m}$  for D3 (blue) and  $l_D = 1.2 \mu\text{m}$  for D4 (red). (d) Simulation results of photocurrent vs light injection position at biases identical to the experimental values.

We estimated the contact barrier height at  $V_g = 0$  V to be  $90$  meV in device D1 by considering the ratio of the dark conductance at  $V_g = 0$  V and  $V_g = 50$  V (flat band). The Fermi level changes relative to the valence band by

$$\Delta E_F = kT \ln \left( \frac{G_{0V}}{G_{50V}} \right) = kT \ln \left( \frac{56 \text{ nS}}{1.4 \text{ nS}} \right) = 90 \text{ meV}$$

if we assume a  $V_g$ -independent hole mobility (Figure S2a in the Supporting Information). Though this Schottky barrier is important for charge separation at the contact, it only results in a  $4 \text{ k}\Omega$  contact resistance estimated from an ideal thermionic emission model,<sup>29</sup> much smaller than the NW resistance  $\sim 1 \text{ M}\Omega$ , consistent with linear dark  $I$ - $V$  curves (Figure 1b) and four probe measurements. This also explains why the ambipolar conduction is not observed in device D1. A hole barrier height of  $90$  meV implies that the electron barrier height is  $\sim 0.3$  eV, considering a  $0.41$  eV band gap. At high  $V_g$ , though the electrons have a high density and are mobile inside the NW, the contact barrier is too high to allow for thermionic emission. A Fermi level close to the midgap allows for both electron and hole conduction in some ambipolar devices (Figure S2b in the Supporting Information).

Because of the small contact resistance, the voltage drop at the contact can be ignored in the experimental bias range ( $V_b = 0$  to  $0.75$  V). The width of the depletion region is estimated to be

$23 \text{ nm}$  at  $V_g = 0$  V in D1, using the formula

$$w = \sqrt{\frac{2\epsilon\epsilon_0(V_{bi} - V)}{qp}}$$

where  $q$  is the charge of the carrier,  $V$  is the voltage drop at the contact (close to zero),  $V_{bi}$  is the built-in potential due to the Schottky barrier,  $\epsilon$  is the relative dielectric constant, and  $p$  is the hole concentration.<sup>30</sup> Thus, the electric field in the depletion region cannot account for the extension of the photocurrent spot. Therefore, when photoinjection is away from the contact, the photocurrent must be caused by carrier diffusion.<sup>8</sup> The photoinjection induces a local high carrier density area, from where the carriers diffuse to the depletion region and are swept out by the electric field. From the line scans (Figure 3c), the exponential fitting  $I = I_{\text{max}} \exp(-x/l_D)$  of the  $V_g = -10$  V curve yields  $l_D \sim 0.97 \mu\text{m}$ . This length slightly increases with increasing  $V_g$  when  $V_g < 50$  V, possibly due to an increase in the carrier lifetime at lower carrier concentration, which can be explained qualitatively by a band-to-band recombination mechanism. When  $V_g > 50$  V, hole diffusion becomes the limiting factor and a significantly longer hole diffusion length is measured ( $l_D = 3.34 \mu\text{m}$  at  $V_g = 90$  V) (Figure 3b, bottom). The same trend is apparent in another device D2, where the contact barriers are less symmetric (Figure 3d).

An external field along the NWs significantly changes the magnitude of the photocurrent spots. As a bias voltage ( $V_b$ ) was applied while fixing  $V_g = 0$  V and the excitation intensity, the photocurrent at the positive (negative) contact was enhanced (suppressed) (Figure 4a). As discussed earlier, the voltage drop at the contact is small at all biases, thus this photocurrent variation is not due to a barrier height change. Instead, the photocurrent change is simply caused by the directional carrier drift under bias, as discussed below. For example, when  $V_b > 0$  V at the left (right) contact, the external electric field causes electrons to drift toward the left (right) and thus increases (decreases) their chance of reaching the contact (Figure 4c, bottom inset). Under all biases, the photocurrent spots are always close to one of the electrodes, consistent with the fact that holes travel much longer than electrons.<sup>11</sup>

At higher bias, we have observed that the photocurrent decays more slowly as the photoinjection position moves away from the contact (as evidenced by the photocurrent line scans normalized by the peak values in Figure S3a in the Supporting Information). As seen in the semilog plot of the line scans (Figure 4b), the photocurrent decreases exponentially away from the peak near the left contact. Remarkably, the decay length increases with increasing bias in our PbS NW FETs (Figure 4c). In device D3, the decay length increases from  $1$  to  $3.3 \mu\text{m}$  when the bias is increased from  $0$  to  $0.75$  V. We attribute this bias-dependent decay length to the carrier drift under an external field. At small bias, the carrier transport is dominated by diffusion, while the carrier drift becomes important at large bias (Figure 4c inset). The crossover from diffusion to drift dominance occurs when the applied electric field is stronger than the diffusion field ( $k_B T/q l_D$ ). Under large electric field, the photocurrent decay length equals the carrier drift length,  $l_E = \mu \tau E$ , which is proportional to the electric field. The dependence of decay length on the field is different than the observations in CdS and Si NWs, where it is independent of the bias.<sup>8,11</sup> This difference may be understood by considering the electric field distribution along the NWs. In CdS NWs, the carrier concentration is very low and the

electric field appears only to be large at the injection area. In Si NWs, the electric field is mainly at the Schottky contact. In both cases, the electric field inside the NWs is small and does not change significantly with bias. On the other hand, in our PbS NWs, the electric field is distributed evenly and the illumination does not significantly change this distribution.

To quantitatively understand this field-dependent decay length, one has to solve the coupled carrier continuity and electrostatic equations with proper boundary conditions. A simple theoretical model has been developed by Rvykin in the 1960s for carrier transport in a nonuniformly illuminated semiconductor with the assumption of charge neutrality.<sup>31</sup> This neutrality is disturbed when minority carriers (electrons) are locally introduced in a p-type semiconductor and is reestablished by a redistribution of the majority carriers (holes) in a very short time. Under a uniform electric field, the distribution of the photogenerated minority carrier density in the steady-state case decreases exponentially ( $\Delta n \propto e^{-x/l}$ , where  $x$  is the distance to the injection position) and the decay length is a combination of diffusion and drift lengths, given by

$$l = \frac{2l_D^2}{\sqrt{l_E^2 + 4l_D^2} - l_E} \quad (1)$$

When  $l_D \gg l_E$  at small bias, eq 1 becomes  $l \sim l_D$ , and when  $l_D \ll l_E$  at large bias,  $l \sim l_E$ . The critical transition point is at  $l_D = l_E$ , or  $E = k_B T / q l_D$ . In our SPCM experiment, the measured photocurrent is proportional to the density of photogenerated minority carriers near the junction<sup>32</sup> and our decay length corresponds to  $l$ . Because the Einstein relationship requires

$$l_E = \frac{qE}{k_B T} l_D^2$$

we can fit our data by eq 1 with only one fitting parameter (Figure 4c). The fits of two different devices (the photocurrent line scans of the other device **D4** are shown in Figure S3b in the Supporting Information) yield a similar  $l_D \sim 1 \mu\text{m}$ , corresponding to an electron mobility-lifetime product  $\mu_n \tau_n = 4 \times 10^{-7} \text{ cm}^2/\text{V}$ . The relatively large error for the data points at low electric field is because of the short fitting range, caused by the negative photocurrent spots on the right portion of the NW.

In conjunction with this theoretical model, a simple finite element method was attempted to simulate the bias dependence. The continuity equation for electrons in one-dimensional form is

$$D_n \frac{d^2 n}{dx^2} + \mu_n E \frac{dn}{dx} + n \mu_n \frac{dE}{dx} + G - U = \frac{dn}{dt} \quad (2)$$

where  $G$  is the photogeneration and  $U$  is the recombination of the carriers. Assuming a steady state condition, Ohmic boundary conditions, and a localized Gaussian injection, this differential equation can be simplified to

$$D_n \frac{d^2 n}{dx^2} + \mu_n \frac{V}{L} \frac{dn}{dx} + G - U = 0 \quad (3)$$

$$G = \alpha \frac{I_0}{h\nu} e^{-(x-x_0)^2/2\sigma^2}$$

$$U = \frac{n - n_0}{\tau}$$

The meanings and the values of the symbols can be found in Table 1. The shape and decay lengths of the simulated photocurrent line scans at different biases (Figure 4d) agree reasonably

**Table 1. Physical Parameters Used in Simulation**

symbol	meaning	value
$L$	NW length	$7.0 \mu\text{m}$
$r_w$	NW radius	$50 \text{ nm}$
$D_n$	electron diffusion coefficient	$0.01 \text{ cm}^2/\text{s}$
$\mu_n$	electron mobility	$0.38 \text{ cm}^2/(\text{V s})$
$\alpha$	absorption coefficient at 532 nm	$10^5 \text{ cm}^{-1}$
$I_0$	peak excitation intensity	$15.3 \text{ W/cm}^2$
$\sigma$	Gaussian beam width	$0.51 \mu\text{m}$
$n_0$	dark electron density	$2 \times 10^{14} \text{ cm}^{-3}$
$\tau$	electron lifetime	$1 \mu\text{s}$

well with the experimental data. The experimental peak photocurrent increases more rapidly with bias compared with the simulation results, possibly because of the enhanced charge separation at large bias. A more general theoretical model and physical understanding to explain the electric field dependence of the photocurrent decay length in various 1-D semiconductors with different doping concentrations and surface/contact conditions has yet to be explored.

In summary, we have fabricated FETs incorporating single p-type PbS NWs with hole mobilities up to  $49 \text{ cm}^2/(\text{V s})$ . The conductance of the devices responded to light excitation sensitively, with a zero-bias charge separation efficiency up to 80% and a rise/fall time of less than  $14 \mu\text{s}$ , making it one of the fastest photoresponse times reported in the literature. Using the SPCM technique, we have extracted a minority carrier diffusion length of  $1 \mu\text{m}$ . This long carrier diffusion length has important implications for the design of solar cells based on PbS NWs, suggesting that diameters up to hundreds of nanometers are ideal. For the first time, we observed an increasing photocurrent decay length with increasing bias, signaling a drift-dominant carrier transport in the NWs at high electrical field. A simple theoretical model was successfully employed in order to explain the field-dependent photocurrent decay length in the PbS NWs.

## ■ ASSOCIATED CONTENT

**S Supporting Information.** SEM image and XRD analysis of as-grown PbS NWs, conductance of a single PbS NW FET as a function of gate voltage showing ambipolar conduction, normalized photocurrent line scans of device **D3**, and bias dependent photocurrent line scans from device **D4**. This material is available free of charge via the Internet at <http://pubs.acs.org>.

## ■ AUTHOR INFORMATION

### Corresponding Author

\*E-mail: [yu@physics.ucdavis.edu](mailto:yu@physics.ucdavis.edu).

### Author Contributions

<sup>S</sup>These authors contributed equally to this work.

## ■ ACKNOWLEDGMENT

This work was supported by the U.C. Davis Startup Fund and the Hellman Fellowship. We thank Professor Y. Gu for helpful discussion and M. Caulfield for assistance with experimental measurements. Work at the Molecular Foundry was supported by the Office of Science, Office of Basic Energy Sciences, of the

U.S. Department of Energy under Contract No. DE-AC02-05CH11231. E. Oh acknowledges the Korea Science and Engineering Foundation (KOSEF) grant funded by the Korea government (MEST) (Grant No. R01-2008-000-20756-0).

## REFERENCES

- (1) Wehrenberg, B. L.; Wang, C. J.; Guyot-Sionnest, P. *J. Phys. Chem. B* **2002**, *106*, 10634–10640.
- (2) Konstantatos, G.; Howard, I.; Fischer, A.; Hoogland, S.; Clifford, J.; Klem, E.; Levina, L.; Sargent, E. H. *Nature* **2006**, *442*, 180–183.
- (3) Luther, J. M.; Law, M.; Beard, M. C.; Song, Q.; Reese, M. O.; Ellingson, R. J.; Nozik, A. J. *Nano Lett.* **2008**, *8*, 3488–3492.
- (4) Sargent, E. H. *Nat. Photonics* **2009**, *3*, 325–331.
- (5) Schaller, R. D.; Klimov, V. I. *Phys. Rev. Lett.* **2004**, *92*, No. 186601.
- (6) Ellingson, R. J.; Beard, M. C.; Johnson, J. C.; Yu, P. R.; Micic, O. I.; Nozik, A. J.; Shabaev, A.; Efros, A. L. *Nano Lett.* **2005**, *5*, 865–871.
- (7) Kayes, B. M.; Atwater, H. A.; Lewis, N. S. *J. Appl. Phys.* **2005**, *97*, 11.
- (8) Kelzenberg, M. D.; Turner-Evans, D. B.; Kayes, B. M.; Filler, M. A.; Putnam, M. C.; Lewis, N. S.; Atwater, H. A. *Nano Lett.* **2008**, *8*, 710–714.
- (9) Balasubramanian, K.; Burghard, M.; Kern, K.; Scolari, M.; Mews, A. *Nano Lett.* **2005**, *5*, 507–510.
- (10) Ahn, Y.; Dunning, J.; Park, J. *Nano Lett.* **2005**, *5*, 1367–1370.
- (11) Gu, Y.; Romankiewicz, J. P.; David, J. K.; Lensch, J. L.; Lauhon, L. J. *Nano Lett.* **2006**, *6*, 948–952.
- (12) Freitag, M.; Tsang, J. C.; Bol, A.; Yuan, D. N.; Liu, J.; Avouris, P. *Nano Lett.* **2007**, *7*, 2037–2042.
- (13) Ahn, Y. H.; Tsen, A. W.; Kim, B.; Park, Y. W.; Park, J. *Nano Lett.* **2007**, *7*, 3320–3323.
- (14) Allen, J. E.; Hemesath, E. R.; Lauhon, L. J. *Nano Lett.* **2009**, *9*, 1903–1908.
- (15) Soudi, A.; Dhakal, P.; Gu, Y. *Appl. Phys. Lett.* **2010**, *96*, No. 253115.
- (16) Kim, C. J.; Lee, H. S.; Cho, Y. J.; Kang, K.; Jo, M. H. *Nano Lett.* **2010**, *10*, 2043–2048.
- (17) Doh, Y. J.; Maher, K. N.; Ouyang, L.; Yu, C. L.; Park, H.; Park, J. *Nano Lett.* **2008**, *8*, 4552–4556.
- (18) Reich, S.; Dworak, M.; Hoffmann, A.; Thomsen, C.; Strano, M. S. *Phys. Rev. B* **2005**, *71*, No. 033402.
- (19) Scanlon, W. W. *Phys. Rev.* **1958**, *109*, 47–50.
- (20) Bierman, M. J.; Lau, Y. K. A.; Jin, S. *Nano Lett.* **2007**, *7*, 2907–2912.
- (21) Yang, P.; Fardy, M.; Hochbaum, A. I.; Goldberger, J.; Zhang, M. M. *Adv. Mater.* **2007**, *19*, 3047–3051.
- (22) Lau, Y. K. A.; Chernak, D. J.; Bierman, M. J.; Jin, S. *J. Mater. Chem.* **2009**, *19*, 934–940.
- (23) Wang, J. F.; Gudiksen, M. S.; Duan, X. F.; Cui, Y.; Lieber, C. M. *Science* **2001**, *293*, 1455–1457.
- (24) Jie, J. S.; Zhang, W. J.; Jiang, Y.; Meng, X. M.; Li, Y. Q.; Lee, S. T. *Nano Lett.* **2006**, *6*, 1887–1892.
- (25) Kung, S. C.; van der Veer, W. E.; Yang, F.; Donavan, K. C.; Penner, R. M. *Nano Lett.* **2010**, *10*, 1481–1485.
- (26) Kind, H.; Yan, H. Q.; Messer, B.; Law, M.; Yang, P. D. *Adv. Mater.* **2002**, *14*, 158–160.
- (27) The absorbed photon flux  $F$  was estimated from  $F = I_0 \alpha \pi r_w^2 d_{\text{laser}} / h\nu$ , where the absorption coefficient of PbS at the incident light wavelength, 532 nm, was  $\alpha = 10^5 \text{ cm}^{-1}$ , the radius of the NW was  $r_w = 40 \text{ nm}$ , the diameter of the laser spot was  $d_{\text{laser}} = 1 \mu\text{m}$ , and  $h\nu$  was the incident photon energy.
- (28) McDonald, S. A.; Konstantatos, G.; Zhang, S. G.; Cyr, P. W.; Klem, E. J. D.; Levina, L.; Sargent, E. H. *Nat. Mater.* **2005**, *4*, 138–U14.
- (29) The contact resistance is estimated from  $R_{\text{contact}} = k_B T / q \pi r_w^2 j_0$  and  $j_0 = A^* T^2 \exp(-qV_{\text{bi}} / k_B T)$ , where  $J_0$  is the saturation current density,  $A^*$  is a constant proportional to effective mass (0.25  $m_0$  in PbS), and  $V_{\text{bi}}$  is the barrier height 90 meV.
- (30) Sze, S. M. *Physics of semiconductor devices*, 2nd ed.; Wiley: New York, 1981.
- (31) Ryvkin, S. M. *Photoelectric effects in semiconductors*; Consultants Bureau: New York, 1964.
- (32) The photocurrent density is  $\Delta J = q D_n (\partial \Delta n / \partial x) + q \mu_n E \Delta n \propto \Delta n$ , proportional to the photogenerated minority carrier density, if the photogenerated minority carrier density in the steady-state case decreases exponentially with length ( $\Delta n \propto e^{-x/l}$ ).